

PSFC/JA-12-3

## Mapping Return Currents in Laser-generated Z-pinch Plasmas

M. J.-E. Manuel, N. Sinenian, F. H. S'eguin, C. K. Li, J. Frenje, H. G. Rinderknecht, D. T. Casey, A. B. Zylstra, and R. D. Petrasso

Plasma Science and Fusion Center, Massachusetts Institute of Technology, Cambridge, MA

## F. N. Beg

Department of Mechanical and Aerospace Engineering. UC. San Diego. CA

March, 2012

Plasma Science and Fusion Center Massachusetts Institute of Technology Cambridge MA 02139 USA

The work de- scribed here was done as part of the first author's PhD thesis and supported in part by NLUF/DOE (Grant No. DE-FG03-03SF22691), FSC/DOE (Grant No. DE-FC02-04ER54789), LLE (No. 412160-001G), LLNL (No. B504974), and GA under DOE (DE-AC52-06NA27279). Reproduction, translation, publication, use and disposal, in whole or in part, by or for the United States government is permitted.

## Mapping Return Currents in Laser-generated Z-pinch Plasmas

M. J.-E. Manuel, N. Sinenian, F. H. Séguin, C. K. Li, J. Frenje, H. G. Rinderknecht, D. T. Casey, A. B. Zylstra, R. D. Petrasso
Plasma Science and Fusion Center, MIT, Cambridge, MA
F. N. Beg
Department of Mechanical and Aerospace Engineering, UC, San Diego, CA

(Dated: 27 March 2012)

Dynamic return currents and electromagnetic field structure in laser-generated Z-pinch plasmas have been measured using proton deflectometry. Experiments were modeled to accurately interpret deflections observed in proton radiographs. Current flow is shown to begin on axis and migrate outwards with the expanding coronal plasma. Magnetic field strengths of  $\sim 1$  T are generated by currents that increase from  $\sim 2$  kA to  $\sim 7$  kA over the course of the laser pulse. Proton deflectometry is demonstrated to be a practical alternative to other magnetic field diagnostics for these types of plasmas.

PACS numbers: 52.70.-m, 52.50.Jm, 52.59.Qy Keywords: proton radiography, return current, Z-pinch

There has been significant effort made to measure spatial distributions of current and magnetic fields in Z-pinch plasmas<sup>1–3</sup>. Conventional techniques, namely Faraday rotation and B-dot probes, have limitations as wire Z-pinch plasmas have very high density in the core and significant density and temperature gradients in the coronal plasma. Proton deflectometry can provide information about current strength as well as magnetic field topology in these plasmas.

In this letter, the first spatially resolved measurements of dynamic currents in Z-pinch plasmas have been made using monoenergetic proton deflectometry. Plasma is created by large return currents<sup>4</sup> driven through the supporting stalk structure of laser-irradiated targets. The stalk ablates due to ohmic heating and a Z-pinch plasma forms with an azimuthal, self-generated magnetic field. The laser interaction with the target produces a positive potential<sup>5</sup> on the target assembly, resulting in a radial electric field on the stalk. The strength and location of these electromagnetic fields has been determined using monoenergetic proton deflectometry.

Experiments were performed at the OMEGA<sup>6</sup> laser facility using the configuration shown in Figure 1a. A thinglass capsule filled with equimolar D<sup>3</sup>He gas was driven by 20 beams to produce fusion protons. This implosion generates monoenergetic DD and D<sup>3</sup>He fusion protons in a quasi-isotropic manner as demonstrated<sup>7-10</sup> in many experiments. The fusion burn region has an approximately Gaussian radial profile with a FWHM of  $\sim 45$  $\mu m^7$  and a burn duration of ~150 ps. Only DD protons were used in these experiments and a sample spectrum is shown in Figure 1b. An upshift in energy is observed due to the positive potential<sup>11,12</sup> on the backlighter capsule during proton production. A detailed schematic of the target assembly is shown in Figure 1c with typical dimensions and materials listed. The resultant Z-pinch plasma was radiographed on a CR-39 plastic nuclear track detector. Proton fluence and relative energy images were generated from processed<sup>13,14</sup> CR-39 samples.

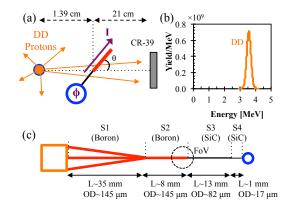


FIG. 1. (a) Experimental geometry. The stalk symmetry axis makes an angle  $\theta \approx 39.4^{\circ}$  with the imaging axis which is necessary for net deflections due to B fields. Residual positive charge on the target creates a potential  $\phi$  that drives a current I up the stalk. (b) Sample fusion proton spectrum. (c) An expanded view of the stalk assembly holding the target (not to scale). Approximate lengths (L) and outer diameters (OD) are listed for the Boron (B) and Silicon-Carbide (SiC) fiber components. The approximate field of view is indicated by the dashed circle.

The experimental geometry was modeled using the Geant4<sup>15,16</sup> framework to accurately interpret proton radiographs. Two sample synthetic radiographs are illustrated in Figure 2a. The first case is a simple 140  $\mu$ m diameter boron stalk with no fields. The stalk stops and scatters DD protons as demonstrated by the white 'shadow' in the  $\langle N \rangle$  image. The second Geant4 simulation example presented in Figure 2a has implemented axisymmetric E and B fields. A constant current *I* and linear charge density  $\lambda$  are distributed uniformly within separate cylindrical annuli around the cold stalk. This model approximates a situation where the current preferentially flows in the expanding hot plasma, due to lower resistivity, and the positive potential manifests as a charge im-

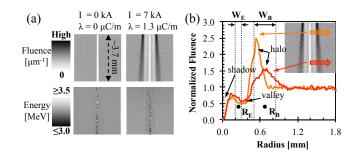


FIG. 2. (a) Synthetic proton radiographs. E and B fields are defined by a linear charge density  $\lambda$  and current *I*, respectively. (b) Fluence lineouts, indicated by arrows, of the second case in a). The mean radii of distributed  $\lambda$  ( $R_E$ ) and *I* ( $R_B$ ) are shown and the widths ( $W_E$  and  $W_B$ ) of the cylindrical annuli indicated by dotted lines. Qualitative lineout features are labeled.

balance. A total of six parameters characterize simulated B and E fields: the current I and charge density  $\lambda$ ; the mean radii of each annulus,  $R_B$  and  $R_E$ ; the corresponding widths,  $W_B$  and  $W_E$ . Assuming an axisymmetric structure, E fields are directed radially outward and B fields are azimuthal around the stalk and vary only as a function of radius. These independently defined parameters determine the appearance of resultant proton radiographs in a specified geometry.

In Figure 2b two fluence lineouts are shown from different positions along the stalk axis (indicated by arrows). In this simulation I=7 kA,  $\lambda=1.3 \ \mu\text{C/m}$  and spatial parameters were set as follows:  $R_B = 675 \ \mu \text{m}, R_E = 250 \ \mu \text{m},$  $W_B=350 \ \mu m$ , and  $W_E=100 \ \mu m$ . An asymmetry is observed due to the differing optical characteristics at locations along the stalk. However, in many cases the qualitative features labeled in Figure 2b may be intuitively explained by the parameters defined in the simulation. Because the angle  $(\theta)$  is not 90°, focusing optics vary along the stalk. Furthermore, to observe a net deflection due to azimuthal B fields the angle  $\theta$  must be  $<90^{\circ}$ . With the current directed away from the target, resultant B fields act to focus protons towards the stalk generating the halo, whereas the positive potential generates electric fields which deflect protons away from the stalk and produce the valley. The precise development of the halo and valley, however, is a result of the combined forces of both B and E fields. For this reason, the relative positions and magnitudes of these forces—as defined by the six input parameters-determine the characteristic features of proton radiographs in a truly coupled manner.

Target stalks were imaged at four different times relative to the onset of the laser drive as indicated (•) in Figure 3a. Both fluence  $\langle N \rangle$  and energy  $\langle E \rangle$  images were generated from DD-proton radiographs and are shown for each sampled time in Figure 3b. In fluence images, darker pixels indicate higher fluence and in energy images, darker pixels indicate lower energy. Because elec-

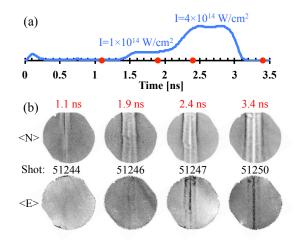


FIG. 3. (a) The picketed laser pulse used on 35  $\mu$ m thick CH shells. Proton arrival times are shown by points lying on the time axis. (b) Proton fluence radiographs  $\langle N \rangle$  taken at four times relative to the laser drive where darker pixels designate higher fluence. The corresponding mean energy images  $\langle E \rangle$  are also shown where darker pixels indicate lower energy.

trons are leaving the target, a residual positive charge is left on the target and stalk with a return current directed as illustrated in Figure 1a. During the pulse, positive charge accumulates and the position and strength of the return current evolves. In some cases, the S3 (SiC) segment of the stalk is not visible, so discussion is limited to the S2 (B) segment in the top of the images (chamber-side). Similar features are observed at the bottom (target-side) of the stalk, though the diameter, material, and optical characteristics are different.

Proton fluence images reveal dynamic E and B field structure over the duration of the laser pulse. The first image in Figure 3b at 1.1 ns shows no sign of the stalk shadow, but a fluence enhancement is observed in its place. This is caused by the return current flowing near the stalk surface, focusing protons to where the shadow would have been. By 1.9 ns, the valley and the halo have become well formed. At 2.4 ns, the stalk shadow has become clearly visible and all of the current flows in the coronal plasma. After the laser pulse has turned off, a strong positive charge and return current are still prevalent. In the last two radiographs, some instabilities are observed jetting out from the stalk; these stochastic features are not modeled.

An iterative procedure was implemented to infer the location and strength of return currents and residual positive charge. The amplitude of features observed in fluence images is directly related to the magnitudes of the current (I) and charge density  $(\lambda)$  through complex electromagnetic optics, though the location and shape are strongly coupled to all parameters. Therefore, a unique solution may be found by achieving reasonable agreement between experimental and synthetic radiographs in the

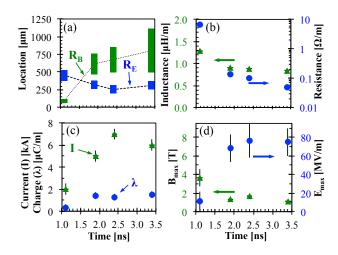


FIG. 4. (a) Location and width of cylindrical annuli for currents and net charge plotted versus time. (b) Estimated inductance and resistance per unit length. (c) Inferred current Iand charge density  $\lambda$ . (d) Corresponding peak field strengths.

specified geometry.

Uncertainties in measurements are estimated based on the sensitivity of synthetic data to variations in input parameters and the variation of experimental data due to different analysis parameters (i.e. lineout width and location). Non-axisymmetric behavior observed in experimental data also contributes some uncertainty to the inferred measurement, but those areas are not used in comparisons with synthetic radiographs. Taking these sources of error into consideration, constant error bars are conservatively estimated to be  $\pm 0.5$  kA and  $\pm 0.3$  $\mu$ C/m for the current and charge density respectively. Uncertainties in spatial parameters  $R_{B/E}$  and  $W_{B/E}$  are not shown in plots, but are estimated to be  $\pm 50 \ \mu$ m.

Measurements of current dynamics are illustrated in Figure 4a. The current annuli, characterized by  $R_B$  and  $W_B$ , were used to calculated the inductance and resistance per unit length, and are shown in Figure 4b as a function of time. To estimate resistivity, the Spitzer form  $(\eta \propto T_e^{-3/2})$  was assumed for a coronal Boron plasma with  $T_e{\sim}1$  keV. It is important to note the low effective of the sector of the low of the sector of the sec tive resistivity per unit length of the plasma  $\sim 0.1 \ \Omega/m$ , as compared to the room temperature measurements of  $\sim 10^8 \ \Omega/m$  for the Boron fiber. From these calculations, an estimated time constant  $(\tau \sim L/R)$  was found to increase from  $\sim 0.2 \ \mu s$  to  $\sim 20 \ \mu s$ . This variability is dominated by the changing resistance of the current carrying plasma. Moreover, these time scales are much longer than any relevant plasma time scales ( $\sim$ ns), indicating that the current will remain well after the  $\sim 3$  ns laser pulse. Although, as the plasma expands and cools, the resistance will increase and the effective decay time decrease, though this does not occur during the sampled time.

3

Measurements of I and  $\lambda$  are shown in Figure 4c. Charge accumulation increases in time eventually flattening out around ~1.3  $\mu$ C/m at 1.9 ns. Furthermore, the resultant return current increases from ~2 kA to ~7 kA at 2.4 ns and slightly decays a few hundred ps after the laser turns off. The current begins near the stalk surface and then preferentially flows outward with the expanding coronal plasma due to the reduced resistivity. Peak magnetic field magnitudes were found to decrease sharply from ~4 T to ~1 T and remained approximately constant throughout the sampled times.

In summary, the first measurements of the dynamic location of current flow in laser-generated Z-pinch plasmas have been made. The feasibility of using proton deflectometry to map electric and magnetic field evolution in a 'single wire'-style Z-pinch configuration has been demonstrated. The skewed angle of the stalk allowed protons to be sensitive to both self-generated electric and magnetic fields. For currents of a few kA,  $\sim 3$  MeV protons provided a reasonable amount of deflection without leaving the field of view. If larger currents were present, higher energy protons would be needed to properly map the field evolution. The model discussed provided an absolute measure of current and charge accumulation while capturing the important effects on proton deflections. In these experiments, return currents were measured and found to increase from  $\sim 2$  kA to  $\sim 7$  kA during a picketed laser pulse. Observations made herein motivate further investigation of dynamic current flow measurements in larger machines, such as the Z-Accelerator. Furthermore, short-pulse proton radiography with Z-Beamlet could provide high temporal and spatial resolution of field structure in advanced pinch configurations at Z.

## ACKNOWLEDGMENTS

The authors would like to express their gratitude to the engineering staff at LLE for their support. The work described here was done as part of the first author's PhD thesis and supported in part by NLUF/DOE (Grant No. DE-FG03-03SF22691), FSC/DOE (Grant No. DE-FC02-04ER54789), LLE (No. 412160-001G), LLNL (No. B504974), and GA under DOE (DE-AC52-06NA27279).

- <sup>1</sup>F. N. Beg, et al. Plas. Phys. Cont. Fus., **39** (1997).
- <sup>2</sup>S. N. Bland, et al. Rev. Sci. Instrum., 77, 10E315 (2006).
- <sup>3</sup>V. V. Ivanov, et al. Phys. Rev. Lett., **97**, 125001 (2006). PRL.
- <sup>4</sup>R. F. Benjamin, et al. Physical Review Letters, **42**, 890 (1979).
- <sup>5</sup>J. S. Pearlman et al. Applied Physics Letters, **31**, 414 (1977).
- <sup>6</sup>T. R. Boehly, et al. Optics Communications, **133**, 495 (1997).
- <sup>7</sup>C. K. Li, et al. Phys Rev Lett, **97**, 135003 (2006).
- <sup>8</sup>J. R. Rygg, et al. Science, **319**, 1223 (2008).
- <sup>9</sup>C. K. Li, et al. Science, **327**, 1231 (2010).
- <sup>10</sup>F. H. Seguin, et al. Physics of Plasmas, **19** (2012).
- <sup>11</sup>D. G. Hicks, et al. Physics of Plasmas, 7, 5106 (2000).
- $^{12}\mathrm{F.}$  H. Séguin, et al. Rev Sci Inst<br/>, $\mathbf{74},\,975$  (2003).
- <sup>13</sup>M. J. Manuel. Rev. Sci. Instrum., 82, 095110 (2011).
- <sup>14</sup>N. Sinenian, et al. Rev. of Sci. Instrum., 82, 7 (2011).
- <sup>15</sup>S. Agostinelli, et al. Nuc Inst Meth A, **506**, 250 (2003).
- <sup>16</sup>J. Allison, et al. IEEE Trans Nuc Sci, **53**, 270 (2006).